Naval Research Laboratory

Washington, DC 20375-5320

Error Analysis of Airborne LiDAR Retro-Reflection Measurements

JEREMY MURRAY-KREZAN

Applied Optics Branch
Optical Sciences Division

November 24, 2009

REPORT DOCUMENTATION PAGE

Public reporting burden for this collection of information is estimated to average 1 hour per response, including the time for reviewing instructions, searching existing data sources, gathering and maintaining the data needed, and completing and reviewing this collection of information. Send comments regarding this burden estimate or any other aspect of this collection of information, including suggestions for reducing this burden to Department of Defense, Washington Headquarters Services, Directorate for Information Operations and Reports (0704-0188), 1215 Jefferson Davis Highway, Suite 1204, Arlington, VA 22202-4302. Respondents should be aware that notwithstanding any other provision of law, no person shall be subject to any penalty for failing to comply with a collection of information if it does not display a currently valid OMB control number. **PLEASE DO NOT RETURN YOUR FORM TO THE ABOVE ADDRESS.**

1. REPORT DATE *(DD-MM-YYYY)*	2. REPORT TYPE	3. DATES COVERED *(From - To)*
24-11-2009	Memorandum Report	April 2008 - March 2009

4. TITLE AND SUBTITLE

Error Analysis of Airborne LiDAR Retro-Reflection Measurements

5a. CONTRACT NUMBER

5b. GRANT NUMBER

5c. PROGRAM ELEMENT NUMBER

6. AUTHOR(S)

Jeremy Murray-Krezan

5d. PROJECT NUMBER

5e. TASK NUMBER

5f. WORK UNIT NUMBER

7. PERFORMING ORGANIZATION NAME(S) AND ADDRESS(ES)

Naval Research Laboratory
4555 Overlook Avenue, SW
Washington, DC 20375

8. PERFORMING ORGANIZATION REPORT NUMBER

NRL/MR/5660--09-9221

9. SPONSORING / MONITORING AGENCY NAME(S) AND ADDRESS(ES)

Office of Naval Research
One Liberty Center
875 North Randolph Street
Arlington, VA 22203-1995

10. SPONSOR / MONITOR'S ACRONYM(S)

ONR

11. SPONSOR / MONITOR'S REPORT NUMBER(S)

12. DISTRIBUTION / AVAILABILITY STATEMENT

Approved for public release; distribution is unlimited.

13. SUPPLEMENTARY NOTES

14. ABSTRACT

LiDAR data was collected by the Airborne 1 Corporation for the Naval Research Laboratory over a ground set-up that included nine retro-reflective panels. The results of the LiDAR experiment are very promising, demonstrating the ability to discriminate the retro-reflective panels from the grassy background. Interestingly, although a high-discrimination capability was demonstrated, the LiDAR data also exhibited strong signal fluctuations. We investigate the error contributors and their potential effects on measured LiDAR signal levels through an analysis of the system noise, atmospheric properties, and analysis of potential sampling variances, related to system and test parameters of the data collect. The analysis techniques explored with this NRL LiDAR data set aid in planning of future tests and further development of the actively-illuminated taggant concepts.

15. SUBJECT TERMS

LiDAR
Retro-reflector

16. SECURITY CLASSIFICATION OF:			17. LIMITATION OF ABSTRACT	18. NUMBER OF PAGES	19a. NAME OF RESPONSIBLE PERSON
a. REPORT	**b. ABSTRACT**	**c. THIS PAGE**	UL	31	Jeremy Murray-Krezan
Unclassified	Unclassified	Unclassified			**19b. TELEPHONE NUMBER** *(include area code)* (202) 767-9365

CONTENTS

ERROR ANALYSIS OF AIRBORNE LiDAR RETRO-REFLECTION MEASUREMENTS

1. INTRODUCTION

The Applied Optics Branch (Code 5660) at the U.S. Naval Research Laboratory (NRL) develops technology for use in a broad range of tactical and wide area surveillance applications. In addition to Airborne LiDAR, the subject of this report, other systems include high-resolution and hyperspectral systems in the visible through infrared spectral regions for applications ranging from small UAVs to high-altitude standoff aircraft.

Airborne LiDAR is commonly used for terrain mapping. However by measurement of the laser return strength, airborne LiDAR can also be used to generate laser-reflectance imagery. In this paper we present an application of airborne LiDAR, specifically as a search tool for detection of retro-reflecting materials, used as passive markers that strongly reflect the LiDAR-source radiation. This concept is being developed at the Naval Research Lab and other aspects of it are reported in Ref.[1]. The concept has been explored by others, such as Ref.[2], but few demonstrations of the concept have been published and several technical challenges remain unresolved. One of the technical problems that must be explored is how to effectively search over wide areas using a laser, which typically has a narrow sample size. Although, LiDAR mapping is not usually known as a rapid data acquisition tool, it has been used to map out large areas of the world, for example entire states, suggesting that for some search scenarios it may be fast enough. Furthermore, faster LiDAR mapping tools are a current topic of research; next generation technologies are promising to improve coverage rates.

In this paper we present results from a LiDAR data collect conducted for the Naval Research Lab. Several retro-reflecting targets are measured during the LiDAR data collect, providing preliminary data to explore the issues of implementing this technology. Since the retro-reflecting targets are small compared to the LiDAR sampling spot size, they are essentially sub-pixel detected, which produces an even more interesting investigation. The experimental results are shown and a detailed analysis of those results is presented. The tools formulated for this analysis also aid in developing better measurement techniques and better systems for future experiments.

This test was supported by the Office of Naval Research (ONR) 6.2 Base Program Autonomous Wide-Band EM Detection of Hidden Targets. The test was conducted in April 2008. The field test and theoretical tools for error analysis are described in Section 2 and results are discussed in Section 3. Concluding remarks are provided in Section 4.

2. METHODOLOGY

LiDAR data was collected by the Airborne 1 Corp. for the Naval Research Lab. This NRL LiDAR data was collected using an Optech 2025 LiDAR system[3,4]. That system was installed on a Beechcraft King Air 200, and collected data over a 400 acre area, including the Drop Zone at Fort A.P. Hill. Retro-reflecting panels, approximately 12" long by 8"wide Reflexite microprism materials, were placed flat on grass. They are placed flat in an attempt to maximize the LiDAR detections. In Figure 1, the first-pulse measured intensity is displayed in color on a geo-rectified (lat/lon) grid. Ground truth verifies that retro-reflectors were placed near where the strongest laser returns are observed.
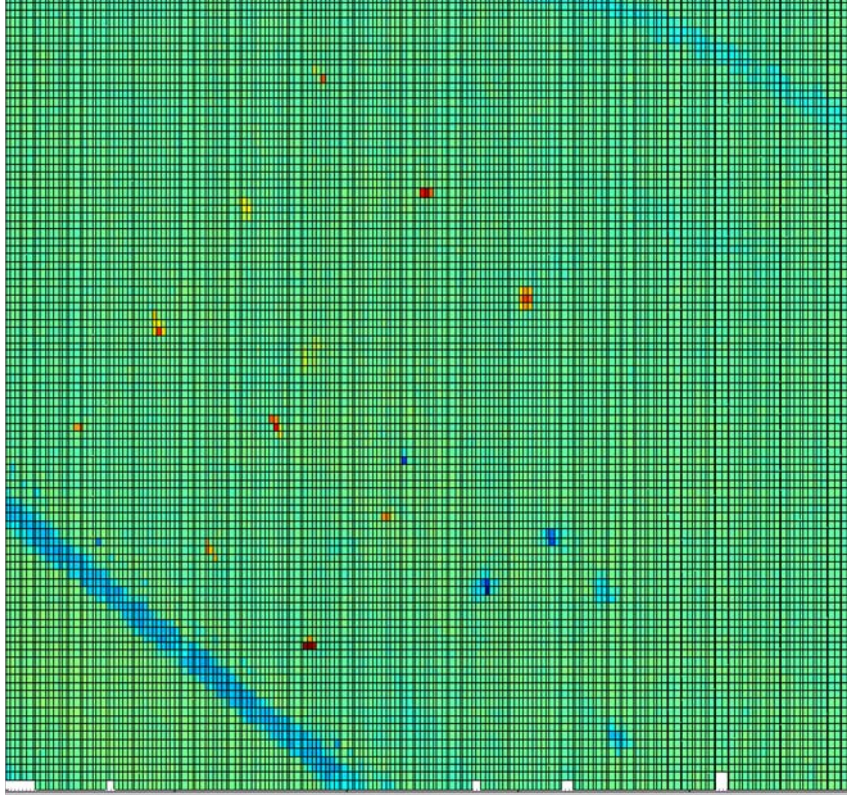
Figure 1: **Measured reflected irradiance from LiDAR measurements. Red is high-reflectance, green is low, and blue is the lowest. The 11 reddest/yellowest data points are verified from ground truth to be near where 11 different retro-reflecting targets were place.**

Although the data in Fig. 1 shows a high level of discrimination from the background, close examination of the retro-reflected LiDAR signal strength reveals that there is significant inconsistency in the results. Figure 2 shows measured levels, which vary between 20 and 270 digital numbers (DNs). A majority of the data is centered around 100DNs. The normalized variance squared σ^2_M is computed according to the following equation:

$$\sigma^2_M = \frac{\langle I^2 \rangle}{\langle I \rangle^2} - 1.$$

For the NRL LiDAR data σ^2_M=0.56. Explanation of the large variation in measured signal levels is a subject of the rest of this paper, where simulation and calculations are used to identify potential noise contributors.
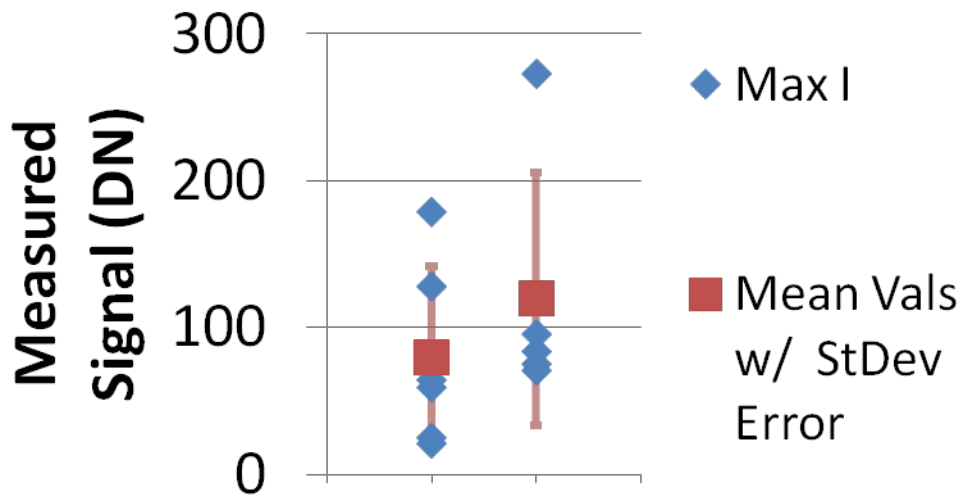
Figure 2: Maximum measured signal intensities within small areas near the known retro-reflector locations are plotted. Data from two differently coated materials are shown, even though we expect that these measurements are insensitive to the coating. A large variation in measured signal levels ($\sigma^2_T=0.56$) is observed.

2.1 Sensor and Experimental Errors

Table 1:

LiDAR System Specifications [3,4]	
Beam Divergence	0.2mrad
Laser Rep. Rate	25kHz
Pulse Duration	7ns
Pulse Energy (Est.)	64mJ
Wavelength	1.064micron
Scan Angle	+/-20 degree
Scan Rate(Est.)	50Hz
Scan Width	2000ft
Altitude	2800ft
Horizontal Accuracy (Est.)	1.4ft
Altitude Accuracy (Est.)	15cm
Range Resolution (Est.)	6.6cm [best 1cm]

Table 1 shows the LiDAR system parameters during the NRL data collect. Several of the results here are estimated based on data obtained from Optech Inc.[3] or Airborne 1 Corp[4].

Detector noise, and other sensor-related noise can cause large fluctuations in signal levels similar to what is seen in the NRL LiDAR data. In addition to sensor-related-noise sources, instabilities in the illuminating-laser system can cause significant fluctuation in received signal levels. For example, in a fielded system potential sources of signal fluctuation, include EMI noise emitted by the airborne or spaceborne platform, and signal fluctuations due to vibrations coupled into inadequately stabilized optics.

 Reference 5 provides a formula for relating the range accuracy, which is provided by Optech and Airborne 1, to the sensor signal to noise. That equation is:

$$\sigma_{Range} = \frac{c}{2} t_{Rise} \frac{1}{\sqrt{S/N}}.$$

Employing that formula, data in Table 1, and an assumption of a 1ns pulse rise time, the best possible sensor and receiver cumulative system SNR is approximately 500.   Additionally, by assuming spatial uniformity of finite areas, where it is reasonable to assume spatial homogeneity, an estimate of the SNR can be obtained. Two examples of SNR in the data are 17.6 for data where the reflected background is grass and 3.7 over a section of road. The corresponding signal levels are, respectively, 11 and 6 digital numbers (DN). These values suggest that the LiDAR sensor related noise is small, less than 2 DN.

The smallest measured signal is 2DN, collected when the sensor was pointed at a black IR resolution target. This dark value is consistent with the SNR estimate.

2.2 Atmospheric Modeling

Another potential source for measured-signal fluctuation is atmospheric distortion.   We consider atmospheric distortion in three ways: i) optical attenuation in the atmosphere, ii) path radiance from the sun during daylight operations, and iii) turbulence. The first and second atmospheric effects, considered in Sec. 2.2.1, are time-independent effects. The third effect, turbulence, is related to optical attenuation in the atmosphere, but is a time-dependant effect. Turbulence is treated in Sec. 2.2.2 and its sub-sections.

2.2.1 Radiance Model of Atmosphere

We model path radiance and time independent atmospheric transmission with PLEXUS, which performs calculations using MODTRAN. PLEXUS is a graphical user interface (see Fig. 3) that facilitates usage of MODTRAN, which is a widely accepted atmospheric modeling tool. The measured at-sensor energy, L, is defined as:

$$L(x,y) = A \iint g\rho(x,y)E_1\tau_{S\to G}\tau_{G\to S} \, dtd\lambda$$
$$+ A \iint (g[\rho(x,y)E_0\tau_{TA\to G}\tau_{G\to S} + \rho(x,y)(L_{TA\to G})\tau_{G\to S} + (L_{G\to S})]) \, dt \, d\lambda,$$

$$(1)$$

where $\tau_{S\to G}$ is the transmittance through the atmosphere between sensor and ground, $\tau_{G\to S}$ is transmittance through the atmosphere between the ground and sensor,   and $\tau_{TA\to G}$ is transmittance through the atmosphere along the path that begins at the top of the atmosphere and ends at the ground. The parameter A is the receiver's area, g is the optical transmittance of photons through the receiver, ρ is the reflectance of the target or background, whichever is located at the sampled ground position, (x,y), $L_{G\to S}$ is the up-welled path irradiance, $L_{TA\to G}$ the down-welled path irradiance; finally E_0 and E_1 are the solar irradiance and laser irradiance respectively. Note, coherent and incoherent radiation are treated in exactly the same way. The difference between coherent and incoherent radiation causes a constant multiplicative factor difference due to summation over different polarization states along the propagation direction. That constant multiplicative factor does not change the signal variance, which is the relevant product of our

atmospheric studies. Most of the parameters in Eq. 1 have explicit wavelength dependence, the exception being A, which only depends on the optical receiver.
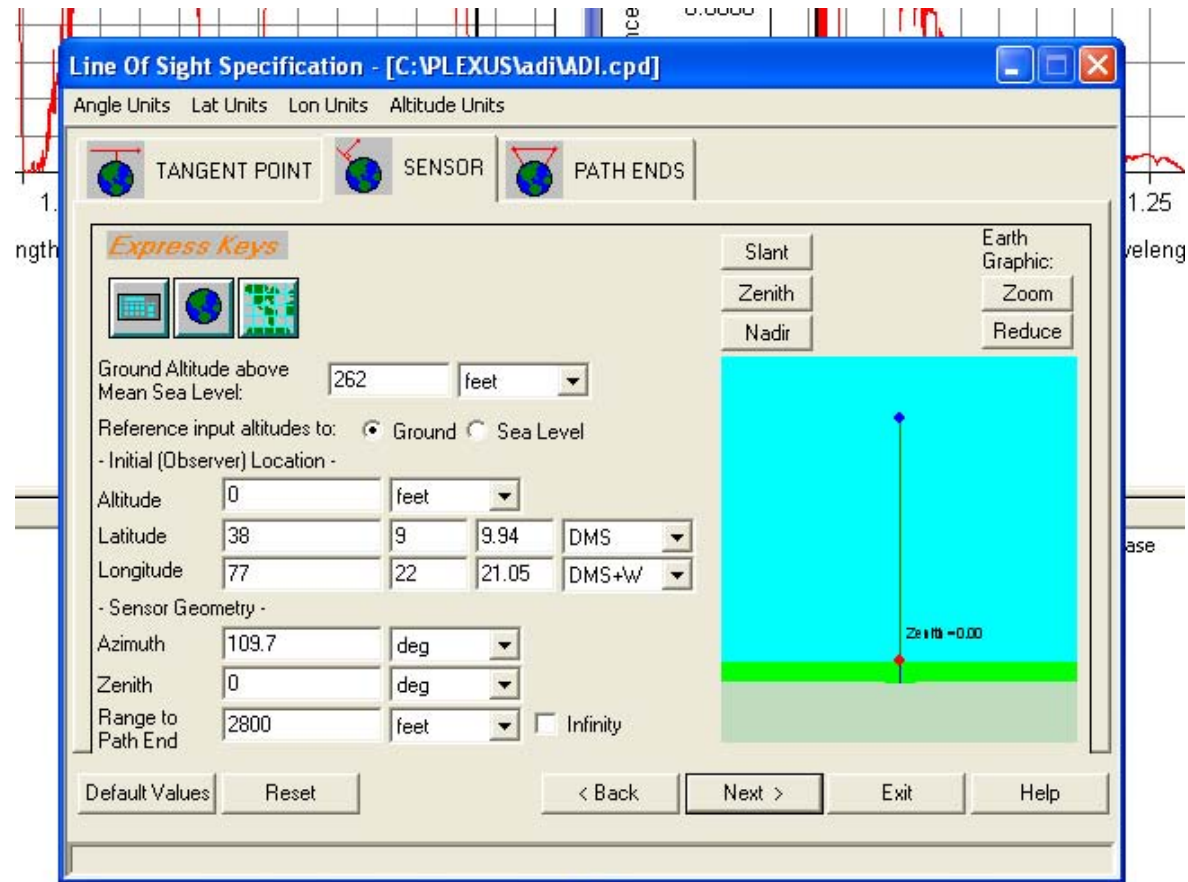

Fig. 3 PLEXUS settings for AP Hill, date chosen to be April 15 2008.

Table 2: L of Eq. 1 is represented here as L_B and L_T for modeled backgrounds and modeled targets respectively.

Model	Description	Scattering	Visibility	L_B	L_T	$L_{G\rightarrow S}$
1	Daytime Top of atm→ ground	Multi; Isaac 2-stream	23km; rural	--	--	$L_{TA\rightarrow G}$ =3.3227e-013
2	Daytime sensor→ ground	Multi; Isaac 2-stream	23km; rural	8.9417e-005	2.1194e-009	6.7267e-013
3	Daytime sensor→ ground	Multi; Isaac 2-stream	5km; rural	5.647e-005	1.3385e-009	5.5536e-013
4	Daytime sensor→ ground	Multi; Isaac 2-stream	1km; rural	6.0099e-006	1.4245e-010	2.1749e-013
5	Daytime	Multi; Isaac	50km;	9.439e-005	2.2373e-009	6.8798e-013

	sensor→ ground	2-stream	rural			
6	Daytime sensor→ ground	Multi; Isaac 2-stream	23km; rural	9.439e-005	2.2373e-009	6.8789e-013
7	Daytime sensor→ ground	Multi; DISTORT 8-stream	50km; rural	8.9417e-005	2.1194e-009	6.7224e-013
8	Daytime sensor→ ground	Multi; DISTORT 8-stream	23km; rural	8.9417e-005	2.1194e-009	6.7224e-013
9	Daytime sensor→ ground	Multi; DISTORT 8-stream	5km; rural	5.647e-005	1.3385e-009	5.5173e-013
10	Daytime sensor→ ground	Multi; Isaac 2-stream	23km; rural;just rained	8.9417e-005	2.1194e-009	6.7267e-013
11	Daytime sensor→ ground	Multi; Isaac 2-stream	5km; rural;just rained	5.647e-005	1.3385e-009	5.5536e-013
12	Daytime sensor→ ground	Multi; Isaac 2-stream	50km; rural;just rained	9.439e-005	2.2373e-009	6.8798e-013
13	Daytime sensor→ ground	Multi; Isaac 2-stream	23km; urban; just	8.8589e-005	2.0998e-009	6.6817e-013
14	Daytime sensor→ ground	Multi; Isaac 2-stream	23km; urban	8.8589e-005	2.0998e-009	6.6817e-013
15	Daytime sensor→ ground	Multi; Isaac 2-stream	5km; urban	5.343e-005	1.2664e-009	5.3042e-013
16	Daytime sensor→ ground	Multi; Isaac 2-stream	5km; urban; just rained	5.343e-005	1.2664e-009	5.3042e-013

Since the exact state of the atmosphere can only be estimated, we use Eq. 1 and all reasonable parameterizations of the atmosphere that also fit with our data collection parameters and flight envelope. The results of this set of parameterizations of the atmosphere bound the noise contributions from atmospheric transmittance and path radiance. Table 2 summarizes these calculations and Fig. 4 graphically exhibits the path radiance results. It is clearly seen in Fig. 4 that the path radiance contribution is negligible compared to the total measured energy- both background scattered energy and target scattered energy. It is expected that the path radiance contribution is small since the sensor is time gated. Comparison of all target scattered data with all other target scattered data suggests that there is less than a factor of two variation due to atmospheric transmission. The same results apply for the background scattered data. This factor of two is due mainly to visibility differences. Realistically, a factor of two variation for our data is unlikely, since visibility is well known (assumed to be 25Km

according to weather data from the day of the collect). Therefore, based on the provided data we estimate the variance contribution due to either path radiance scattering, or optical transmission to be negligible, less than 1DN. Variance due to time dependant changes, specifically turbulence are addressed in the next section.
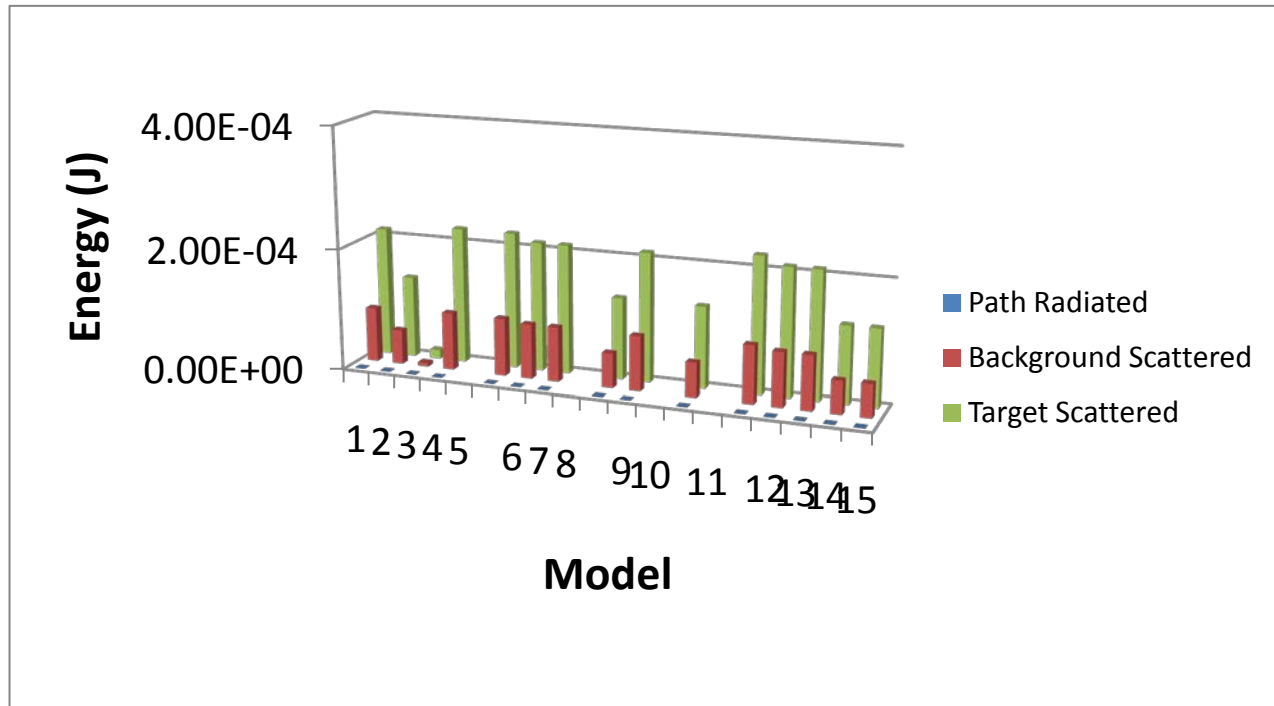

Fig. 4: Static atmospheric results calculated with PLEXUS/MODTRAN. Several models are used with parameters defined in Table 2. Energy in this chart is calculated using the Table 2 model radiance results, and sensor/scene model parameters. The results indicate clearly that path radiance scattering contributes little compared to background scattered or target scattered radiation.

2.2.2 Turbulence Model of Atmosphere

The term turbulence refers to time dependent changes in the atmosphere. Optical transmission of a laser through turbulent media is a widely studied field. We leverage that body of knowledge for estimation of turbulence's effect on our measurements, providing order of magnitude estimations of turbulence-induced irradiance variations. We use two references [6,7] to develop two different estimates on the effects of turbulence. Two different methods are used so that the estimates can be explored from multiple perspectives. Additionally, since neither computational method is specific the NRL LiDAR measurements, usage of two independent techniques aids in checking the verity of results. The first reference is a peer-reviewed journal article by Ferdinandov, Tsanev, and Todorov [6]. In their article Ferdinadov et al. utilize a heuristic model of the atmosphere and a contrast model of a target and background to mathematically derive the signal to turbulence noise ratio. In that effort, an infrared laser sensor is pointed down from an altitude of H<3km. The second reference used to model LiDAR performance when sensing through a turbulent atmosphere is the text book by Andrews and Phillips [7]. In that book, infrared laser satellite communications from 38,000km to ground are explored. There,

several concepts are discussed in detail that allows us to relate the laser communications problem that they explore to the LiDAR problem that we investigate.

2.2.2 A Ferdinandov Turbulence Model

As previously mentioned, the methods of Ferdinandov et al.[6] supply a heuristic model for calculation of signal to turbulence noise in LiDAR experiments. In Ferdinandov's article the atmosphere is considered to be a collection of small spherical lenses that act to both focus and/or scatter laser light. The variance of the irradiance amplitude level, σ_χ^2, is calculated using equation 2. In equation 2, γ is visibility, H is the LiDAR sensor altitude above the ground/target, h is a parameter of altitude that ranges from zero at ground level to H at maximum, $C(h)_n^2$ is the atmospheric structure constant at altitude h, and k=$2\pi/\lambda$ where λ is the laser wavelength. Using the variance of irradiance amplitude level, the contrast in irradiance is given by equation 3, assuming that χ is a normally distributed random value. In accordance with these equations, the irradiance, E, obeys a lognormal distribution law. We calculate the contrast of irradiance when light travels through a turbulent atmosphere described by parameters given in the caption of Fig. 5; this plot reproduces, for comparison, figure 5 of Ref. [6].

$$\sigma_\chi^2 = \frac{2^{3/4}}{3\gamma} C(0)_n^2 k^{7/6} H \left[\frac{1+\gamma H}{\gamma H} \ln(1 + \gamma H) - 1 \right] \quad (2)$$

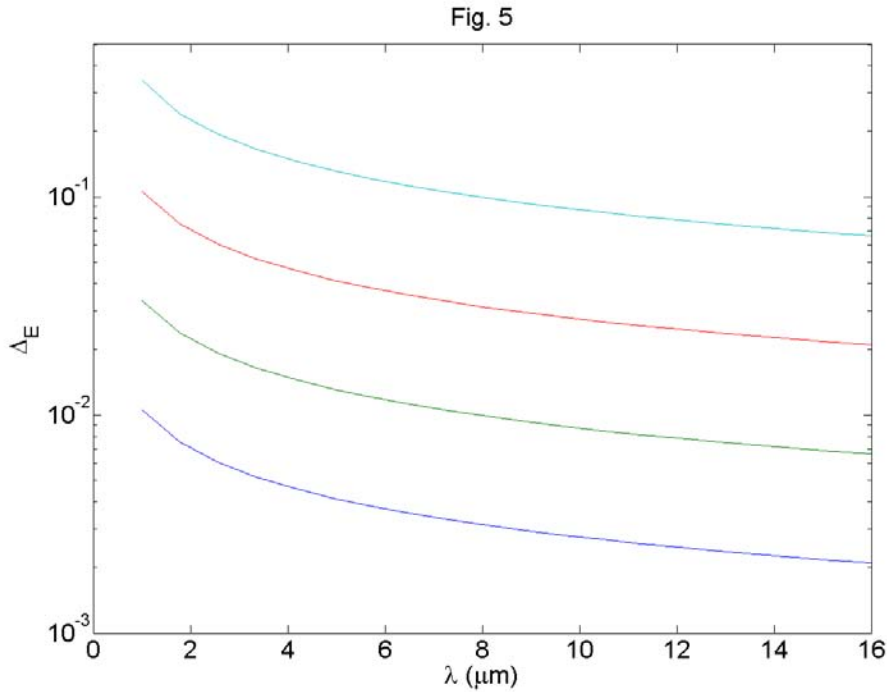$$\Delta_E = \sqrt{\exp\left(4\sigma_\chi^2\right) - 1} \quad (3)$$

Fig. 5: Reproduces Fig. 5 of Ferdinandov[6]. Family of curves with, atmospheric structure constant $C_n^2(0) = 10^{-14}$, $C_n^2(0) = 10^{-15}$, $C_n^2(0) = 10^{-16}$, and $C_n^2(0) = 10^{-17} m^{-2/3}$, from top to bottom. Other parameters used here are range to scatterer H=1km, detector size a=100micrometers, receiver focal length f=1000m, visibility $\gamma = 8km^{-1}$.

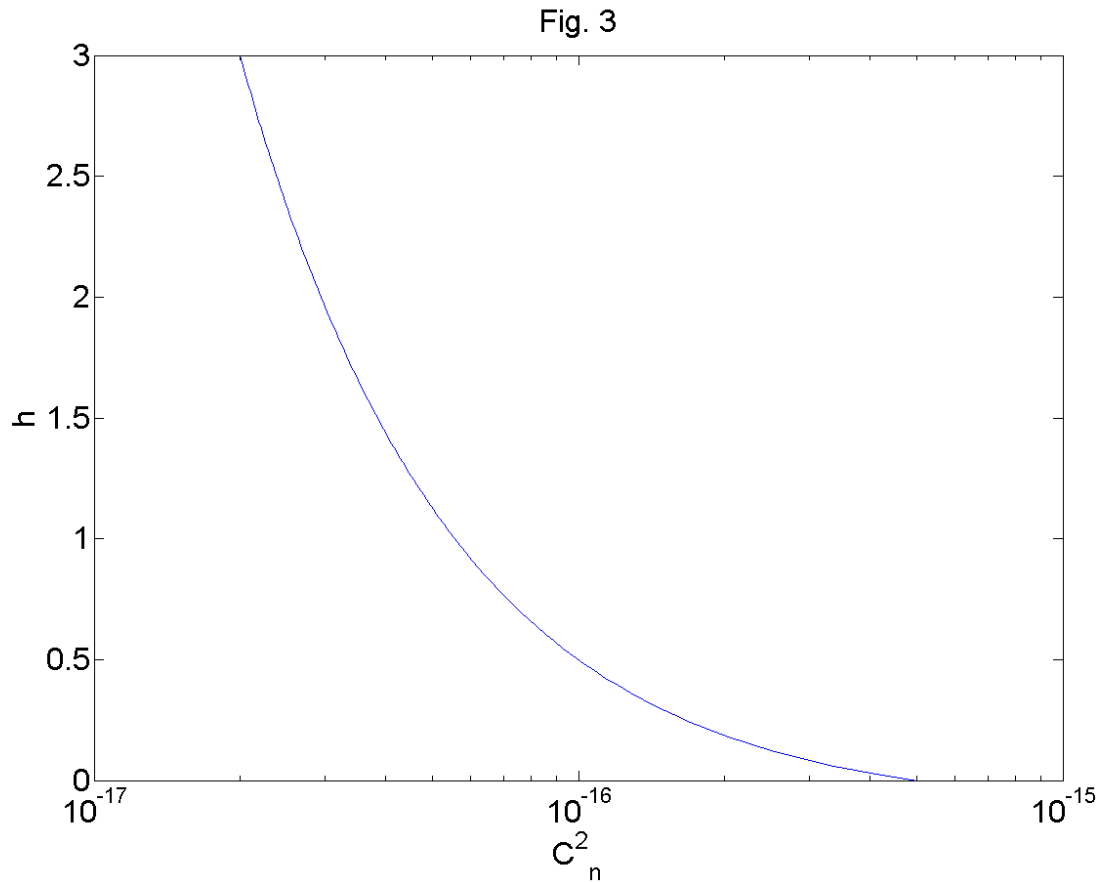The definition of γ that we use is verified by reproduction of Ferdinandov's figure 3, plotted in Fig. 6.

Fig. 6: Plot of Ferdinandov's equation 3 and replication of Fig. 3[6]. Here gamma=8km^{-1}, and $C_n^2(0)$=5x10^{-16}.

The parameter x is called the degree of averaging effect, which affects the measured contrast, Δ_φ. Equation 4 describes x mathematically. The degree of averaging effect is dependent on the ratio of the sample distance (A) to the correlation radius of irradiance through turbulent fluctuations (r_E). This is represented in Fig. 6 of Ferndinandov, reproduced here in Figs. 7 and 8, with parameters described in the captions.

$$x\left(\frac{A}{r_E}\right) = \left.\left(\frac{A}{r_E}\right)^2 \middle/ \left[\sqrt{\pi}\left(\frac{A}{r_E}\right)erf\left(\frac{A}{r_E}\right) + exp\left(-\frac{A^2}{r_E^2}\right) - 1\right]\right. \tag{4}$$

$$r_E = 0.47\sqrt{H\lambda}$$

$$A = \frac{a}{Hf}$$

Fig. 6

Fig. 7: Reproduction of data in Ferdinandov's Fig.6[6], with detector size a=100x10^{-6}m, focal length f=1m, H=1km. Squares are when A/r$_E$ ranges over λ=1-16 microns. Blue dots are when A/r$_E$ ranges between 10^{-3} and 10.
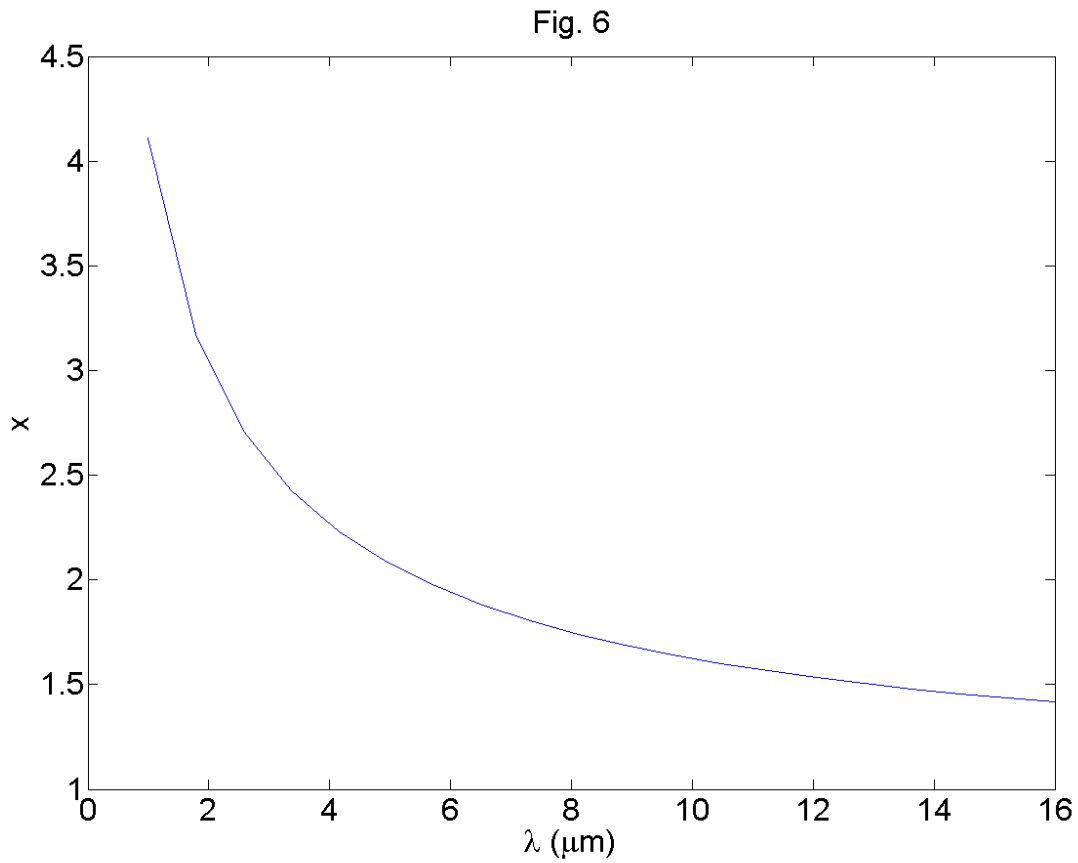
Fig. 8: Reproduction of Ferdinandov's Fig.6[6], with same parameters as in Fig. 5[6].

Ferdinandov's final result is a calculation of the signal to turbulence noise ratio(SNTR). See Eq. 5 for expressions describing STNR, generated as a function of the spatial contrast at the scattering plane, Δ_α (when h=H), and the measured contrast, Δ_φ, which is a function of the irradiance flux through the receiver. Note Δ_φ is related to the irradiance flux through the atmospheric turbulence, Δ_E, and the degree of average effect via Eqn. 6. Δ_α is a fractional number, plotted as a percentage in the Figs.9-11: reproductions of Ref.[6]'s figure 7.

$$SNTR = \frac{\Delta_\alpha}{\Delta_\varphi} \quad (5)$$

$$\Delta_\varphi = \frac{\Delta_E}{x\left(\frac{A}{r_E}\right)} \quad (6)$$

Fig. 7.1

Fig 9: Reproduction of Fig.7.1 in Ferdinandov[6]; Top to bottom STNR=30, 25, 20, 15, 10, & 5 when $C_n^2(0) = 10^{-16}$.
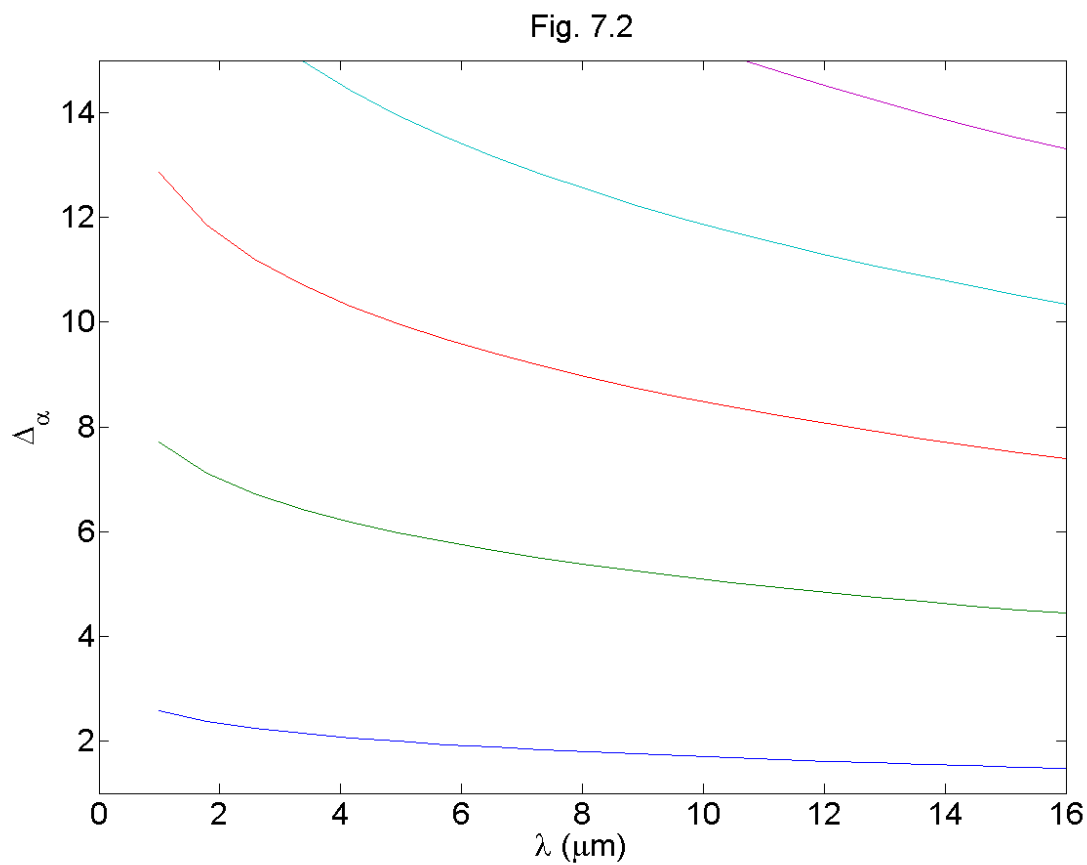
Fig. 10: Reproduction of Ferdinandov Fig.7.2[6]; Top to bottom STNR=9, 7, 5, 3, & 1, when $C_n^2(0)$ = 10^{-15}.
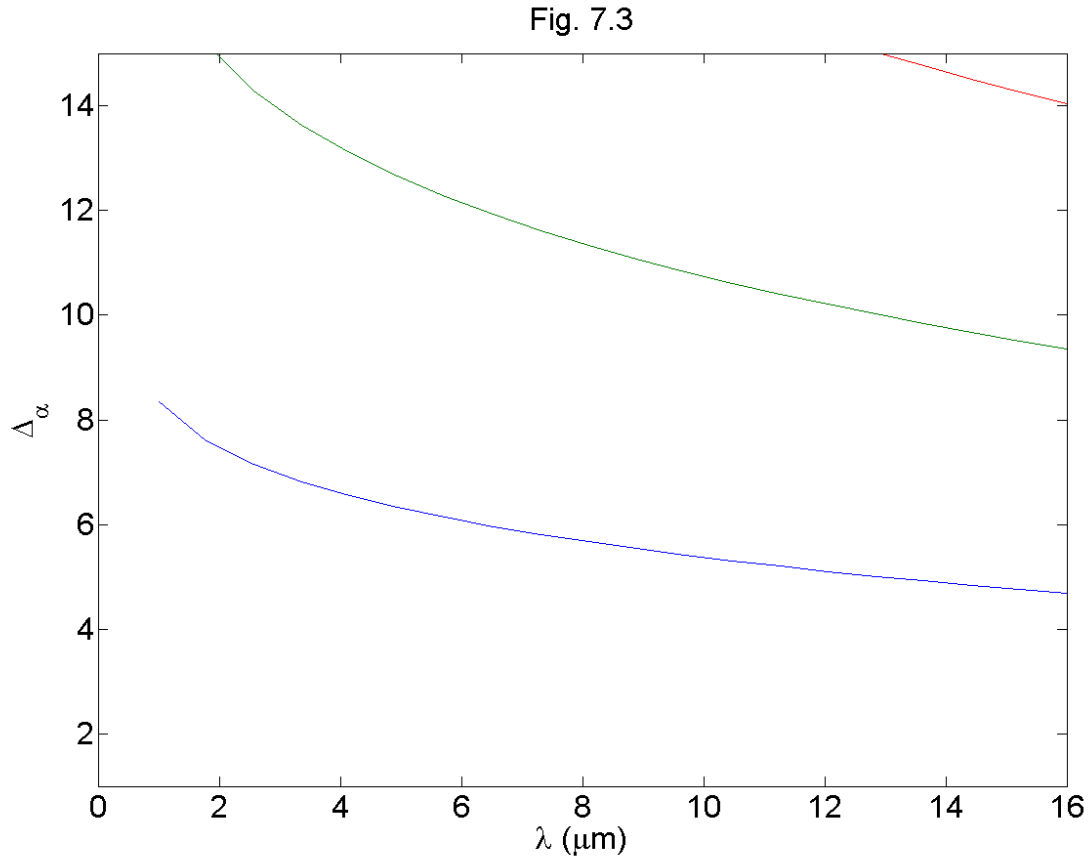
Fig. 7.3

Fig. 11: Reproduction of Fig.7.3 in Ferdinandov[6]; Top to bottom STNR=3, 2, & 1 when $C_n^2(0) =$ 10^{-14}.

2.2.2 B Ferdinandov Model Calculations

We use the Ferdinandov model to simulate the NRL LiDAR measurements. Parameters of our calculations are λ=1.064 microns, a=100x10^{-6}m, f=1000mm, H=2800ft (854m), Visibility = 25km, and the atmospheric structure constant, $C_n^2(0)$, ranges 10^{-17}-10^{-14}. This set of parameters describes Δ_φ, Δ_E and the degree of average effect. Fig. 12 shows the relationship between SNTR and spatial contrast in a general way. From our calculations we find Δ_φ=0.0025-0.0795. This result is an estimate of turbulence induced measured irradiance fluctuations.
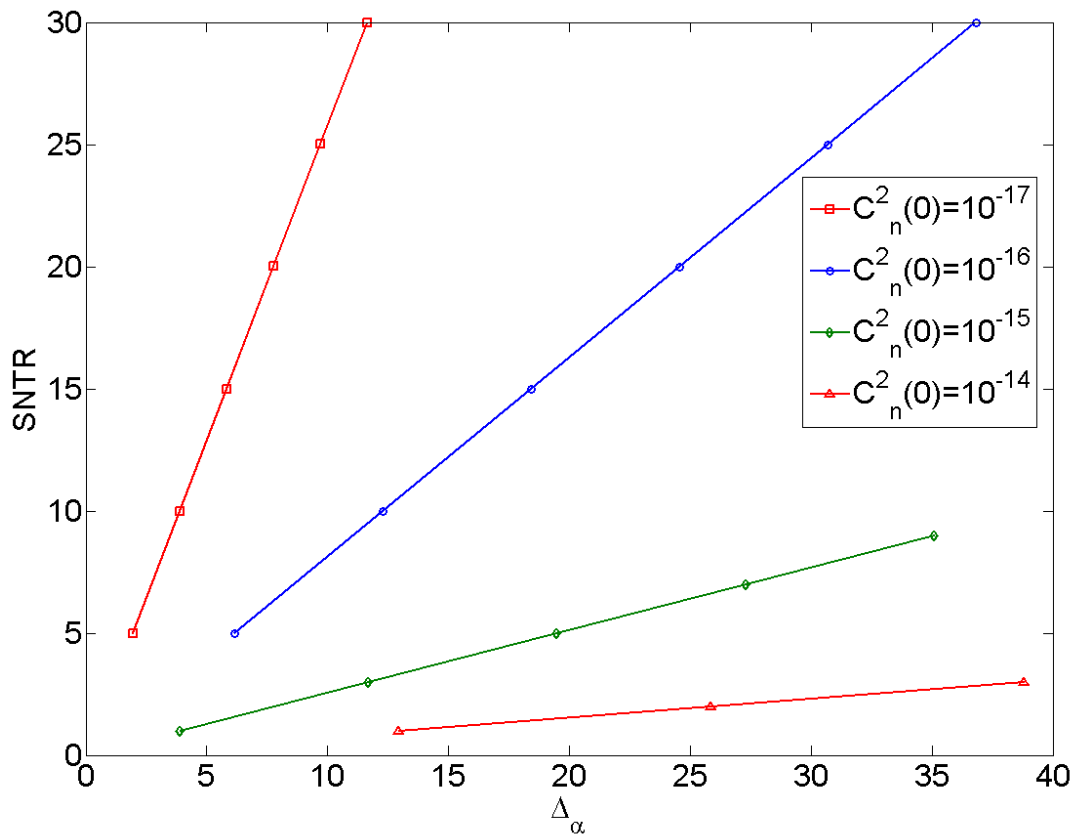
Fig. 12: Result at 25km visibility, λ=1.064μm, H=2800ft. Note, these results are found to be relatively insensitive to visibility.

2.2.2 C Andrews and Phillips Turbulence Model

Andrews and Phillips's text book (Ref. [7]) describes a laser propagating through the atmosphere for the application of laser communications from satellites to ground or vice versa. While Ferdinandov et al.'s work is concise, Andrews and Phillips's work is comprehensive and discusses several issues such as the scintillation index and beam wander.

The beam profile that is used in the Andrews and Phillips model is shown in Fig. 13. In that plot the beam's effective radius, W_e, is shown as a function of the initial beam radius, W_0, for two different zenith angles, ζ. Equations 7-11 describe a Gaussian beam's effective radius after propagating up from the ground. In Ref.[7]'s calculation the propagation distance $H=38.5 \times 10^3$km. The beam's radius of curvature, F_0, is chosen to be infinite, since the beam is collimated. The parameters Θ_0, Λ_0, and Λ are standard parameters that describe a propagating Gaussian beam[8]. The H-V atmospheric model supplies atmospheric simulation parameters. That model is specifically applicable to satellite communications, where the satellite is of course high above the earth's surface.
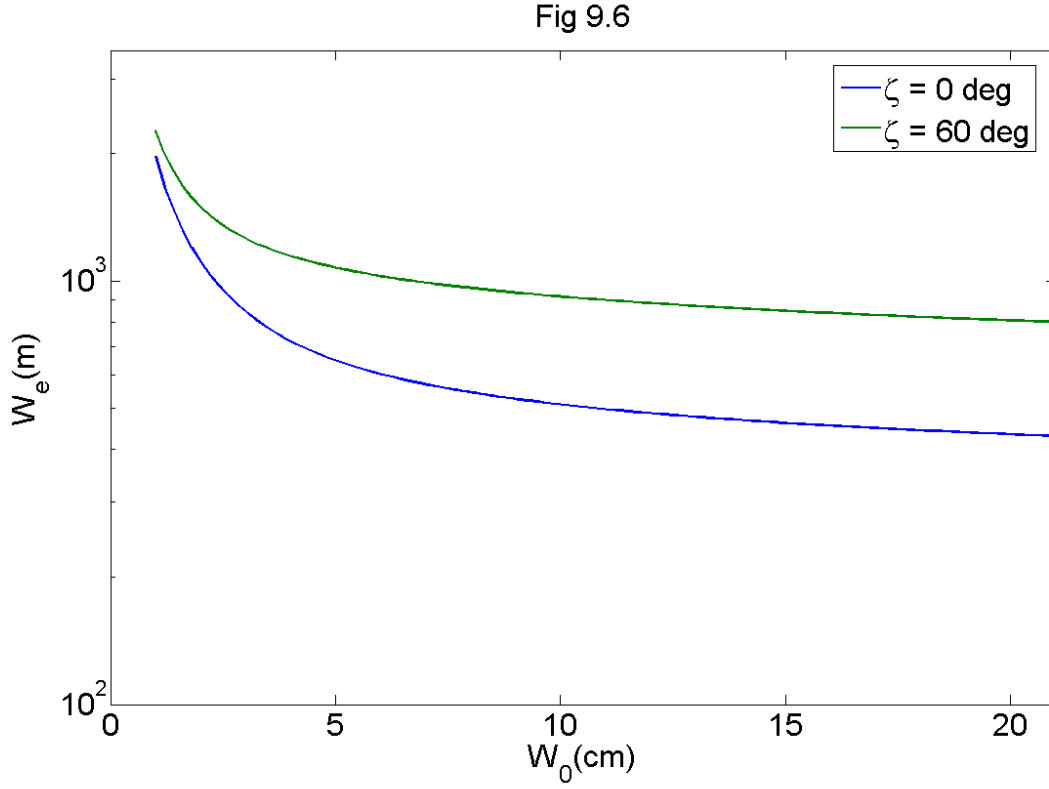
Fig 9.6

Fig 13: Effective beam radius, W_e, plotted as a function of initial beam radius, W_0, for two zenith angles, ζ. This plot reproduces Fig 9.6 of Ref.[7].

$$W_E = W\sqrt{1 + 4.35\mu_2\Lambda^{5/6}k^{7/6}(H-h)^{5/6}\sec^{11/6}(\zeta)} \quad (7)$$

$$\mu_2 = \int_0^H C_n^2(h)\left(\frac{h}{H}\right)^{5/3} dh \quad (8)$$

$$\Lambda = \frac{\Lambda_0}{\Theta_0^2 + \Lambda_0^2} \quad (9)$$

$$\Theta_0 = 1 - \frac{(H-h)}{F_0} \quad (10)$$

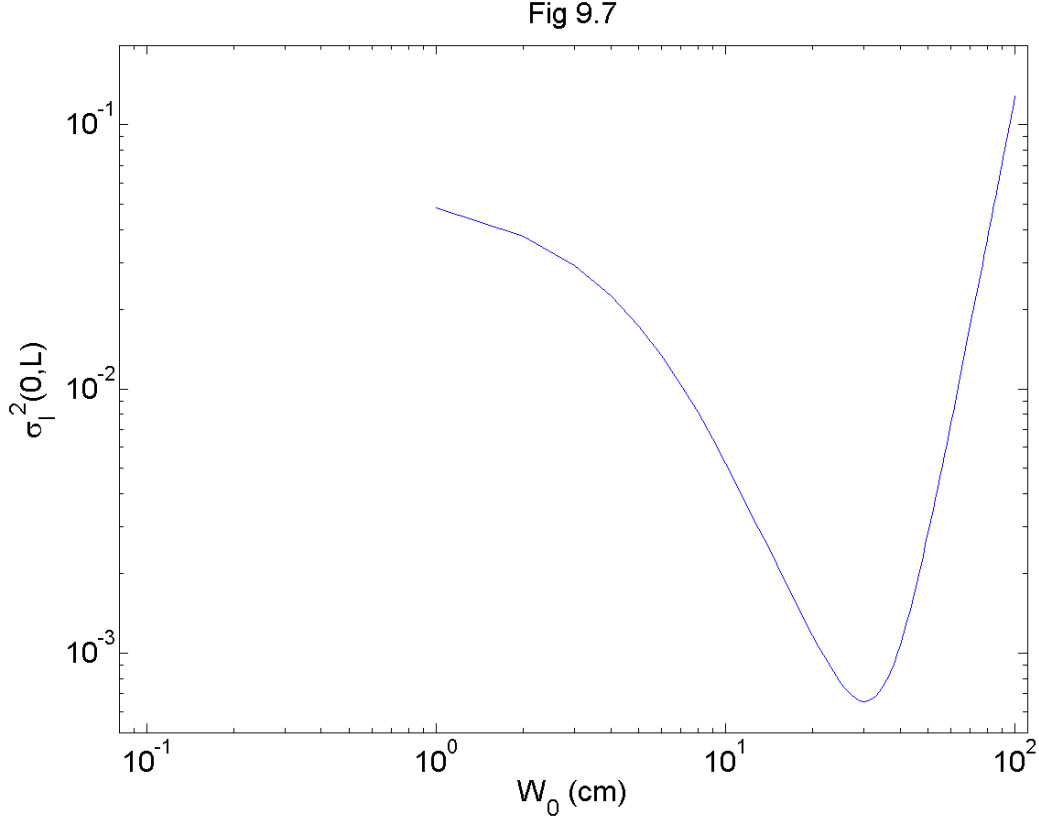$$\Lambda_0 = \frac{2(H-h)}{kW_0^2}. \quad (11)$$

Fig. 14: Reproduction of Figure 9.7 in Ref.[7]. Plotted is the on-axis scintillation index as a function of the initial beam radius, assuming the H-V atmospheric model for an uplink channel satellite communication.

The scintillation index is defined as the $\sigma_I^2(r,H) = \langle I^2\rangle/\langle I\rangle^2 - 1$, which is the variance in measured intensity, normalized by the mean intensity squared. Here r is the off-axis position at which the scintillation index is calculated. Inclusion of the off-axis position r, accounts for potential pointing inaccuracies. The equations that calculate the scintillation index and generate the graphs in Figs. 14 and 15 are:

$$\sigma_I^2(r,H) = \begin{cases} 8.702 k^{7/6} H^{5/6} sec^{11/6}(\xi)\left[\mu_3 + 1.667 \frac{\mu_1 \Lambda^{5/6} \alpha^2 H^2 sec^2(\xi)}{W_0^2(\Theta_0^2+\Lambda_0^2)}\right] (uplink) \\ 8.702 k^{7/6} H^{5/6} sec^{11/6}(\xi)\left[\mu_4 + 1.667 \frac{\mu_2 \Lambda^{5/6} \alpha^2 H^2 sec^2(\xi)}{W_0^2(\Theta_0^2+\Lambda_0^2)}\right] (downlink) \end{cases} \quad (12)$$

$$\mu_1 = \int_0^H C_n^2(h)\left(1 - \frac{h}{H}\right)^{5/3} dh \quad (13)$$

$$\mu_3 = Re \int_0^H C_n^2(h)\left\{\left(1 - \frac{h}{H}\right)^{5/6}\left[\Lambda\left(1 - \frac{h}{H}\right) + i\left(1 - \overline{\Theta}\left(1 - \frac{h}{H}\right)\right)\right]^{5/6} - \Lambda^{5/6}\left(1 - \frac{h}{H}\right)^{5/3}\right\} dh \quad (14)$$

$$\mu_4 = Re \int_0^H C_n^2(h)\left\{\left(\frac{h}{H}\right)^{5/6}\left[\Lambda\frac{h}{H} + i\left(1 - \overline{\Theta}\frac{h}{H}\right)\right]^{5/6} - \Lambda^{5/6}\left(\frac{h}{H}\right)^{5/3}\right\} dh \quad (15)$$

$$\overline{\Theta} = 1 - \Theta \quad (16)$$

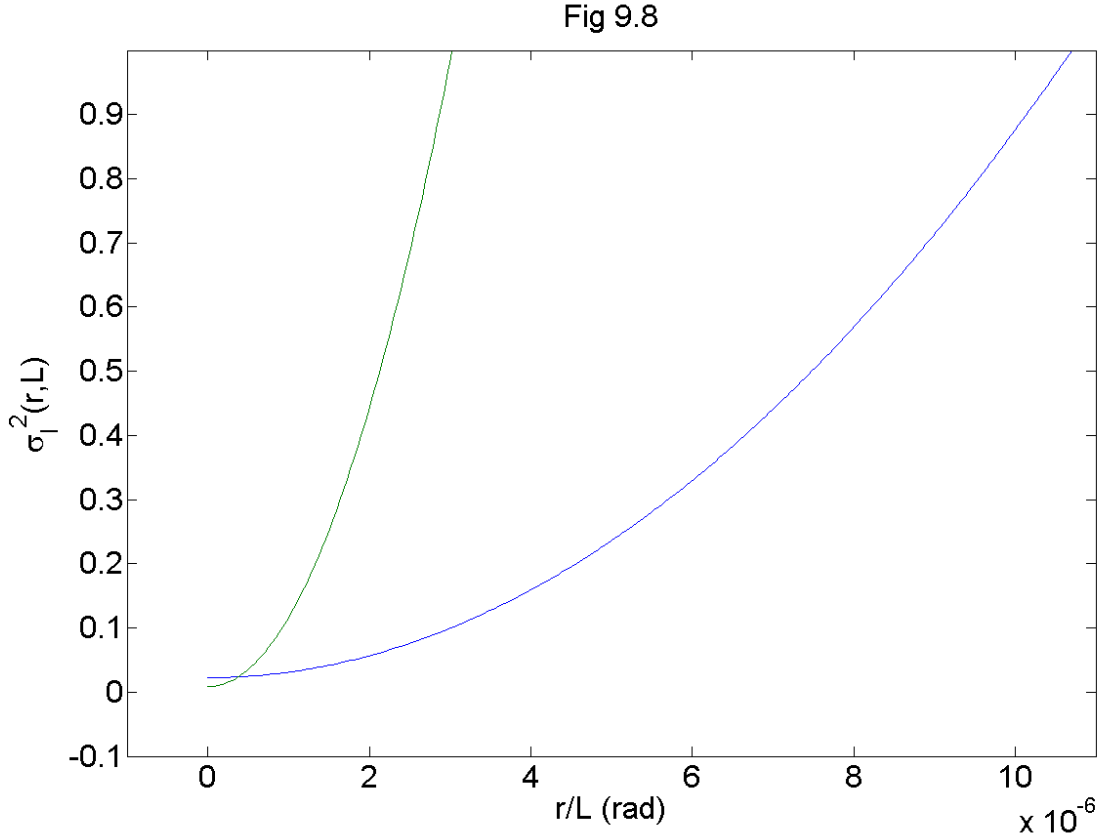$$\Theta = \frac{\Theta_0}{\Theta_0^2 + \Lambda_0^2}. \quad (17)$$

Fig. 15: Reproduces Figure 9.8 of Andrews and Phillips[7], showing again the scintillation index both on and off axis where L=H, the altitude, and r is the off axis position where the scintillation index is calculated. The blue line is for an initial beam radius W_0=4cm, and the green line shows the same for an initial beam radius of W_0=8cm.

The airborne scenario, which is relevant for the NRL LiDAR data, is related to the satellite communication problem with a few reasonable assumptions. The two biggest differences between what the Andrews and Phillips model calculates and what the NRL data measures are i) in the satellite communication model, the source altitude is higher than in the airborne scenario and ii) the satellite communications model is described in two parts: uplinks and downlinks. The first difference called-out suggests no major changes to the model, only a lower source altitude must be used. The second difference mentioned means that the airborne model we apply must be approached in two steps, first the downlink then the uplink.

We use the computational techniques previously applied by Bufton et al.[9] to ground-based laser light that is retro-reflected from a satellite. Bufton's technique assumes multiplicative combination of the laser light variances, satisfying the equation: $I_T = I_{UL}I_{DL}/\langle I_{DL}\rangle$. To combine the downlink beam variance with the uplink beam variance we must assume independence of the normalized variances, $\sigma^2_{DL}(r,H)$ and $\sigma^2_{UL}(r,H)$, and that the background/target scatters the light primarily in the backward direction. Making all of these assumptions then $\langle I_T^2\rangle = \langle I_{DL}^2\rangle\langle I_{UL}^2\rangle - \langle I_{DL}\rangle^2\langle I_{UL}\rangle^2$, which simplifies to:

$$\sigma^2_{Total}(r,H) = \sigma^2_{DL}(r,H) + \sigma^2_{UL}(r,H) + \sigma_{DL}(r,H)\,\sigma_{UL}(r,H). \quad (18)$$

Lambertian scattering is perhaps more appropriate in some cases of reflection, however even with Lambertian scattering *the measured laser light is primarily backscattered*. Assuming a finite radius of

curvature, F_0, for the uplink portion partially accounts for Lambertian scattering. On the other hand, assuming that all light is backscattered assumes more laser light is reflected back to the sensor than is accurate. Whichever the case, the turbulence model of Andrews and Phillips accounts for propagation of light that is measured; implementation of the model only requires accurate data for the model parameters. The measured intensity difference may be accounted for with an effective albedo term, R, reducing the uplink radiance to appropriate levels: $\sigma^2_{Total}(r,H) = \sigma^2_{DL}(r,H) + R\sigma^2_{UL}(r,H) + \sigma_{DL}(r,H)\,\sigma_{UL}(r,H)\sqrt{R}$. This effective albedo term ranges from zero to unity.

2.2.2.D Andrews and Phillips Turbulence Model Calculations

The Andrews and Phillips model supplies intensity variation due to scintillation. Starting from the formulas shown in Sec. 2.2.2.C, we calculate for the NRL LiDAR data, employing the parameters in Table 1. Figure 16 shows the NRL LiDAR beam profile. In Figs. 17 and 18, respectively, the scintillation index is displayed as a function of the angular off-axis-measurement position for an uplink and a downlink.
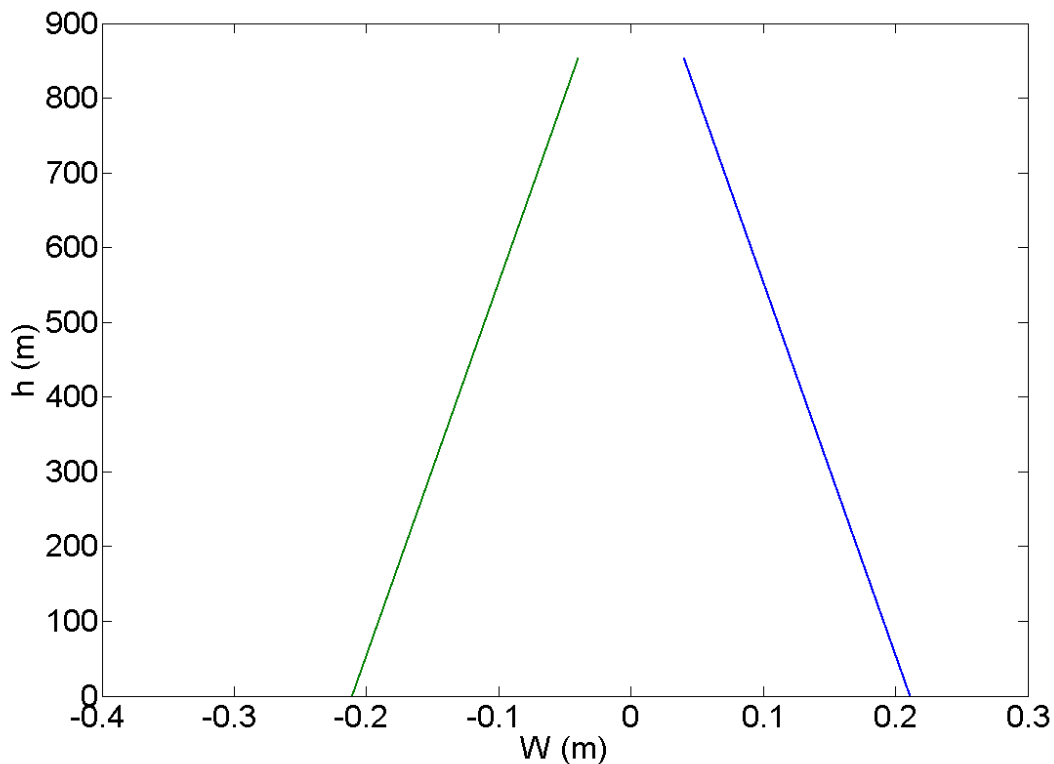

Fig. 16: Beam profile applicable to the NRL LiDAR measurements.

From the Andrews and Phillips model we estimate that the effective beam radius at the ground is approximately 17cm given an initial beam radius of 2cm. The scintillation index in the uplink channel (see Fig. 17) is between 0 and 0.32. In the downlink channel the scintillation index can range between 0 and 0.03.
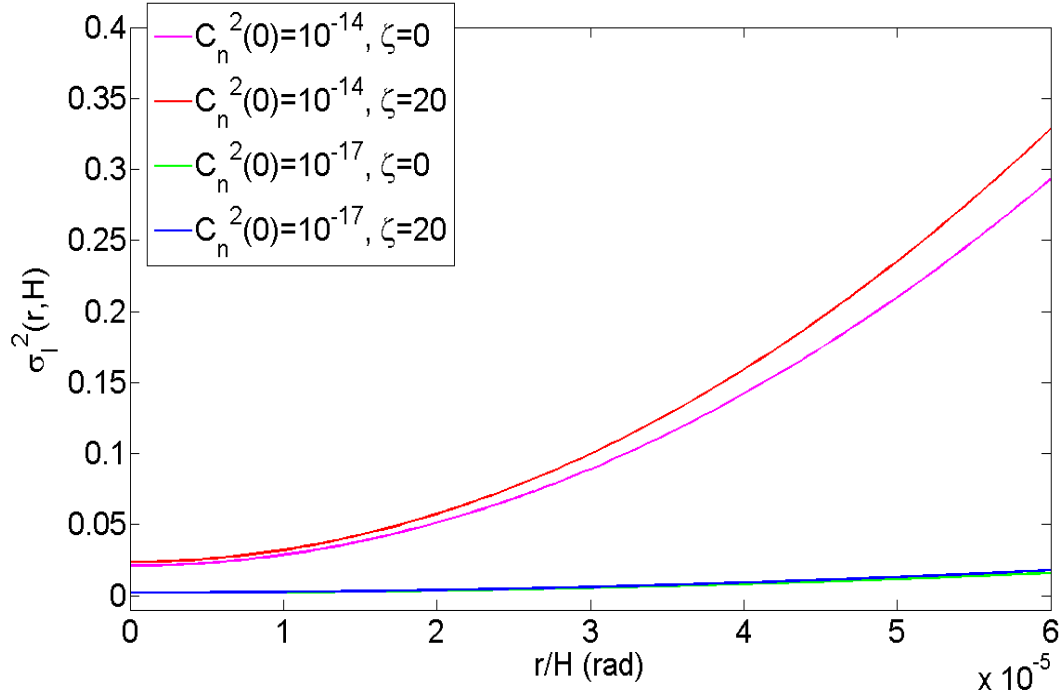
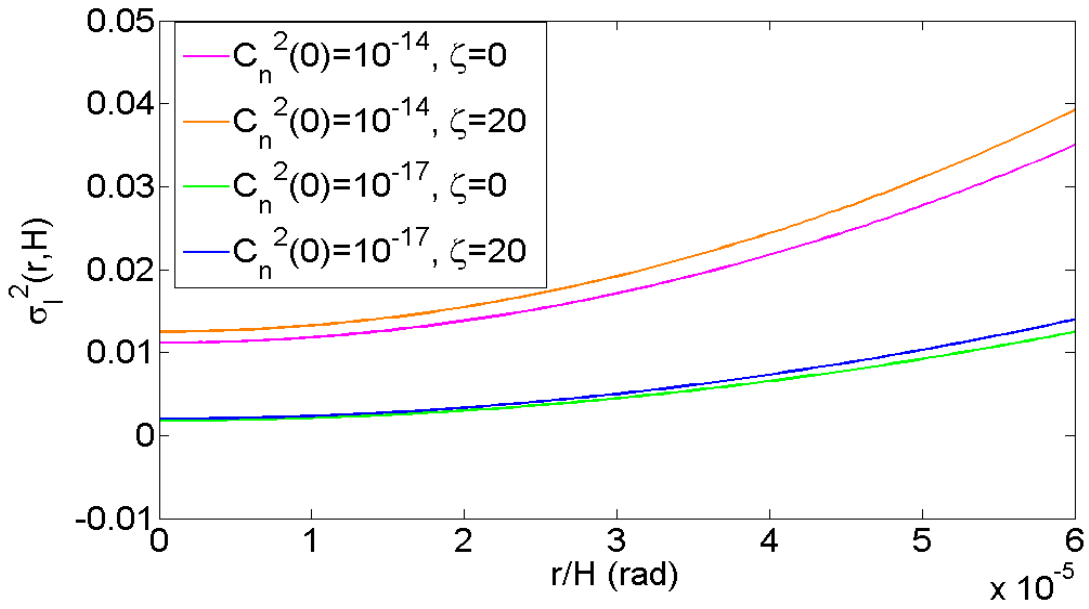Fig. 17: Uplink scintillation index covering the range of possible measurements.

Fig. 18: Downlink scintillation index over the range of possible measurements.

The total scintillation index range is σ_T^2=0-0.4. We acknowledge that kurtosis in the measurements could result in measurement errors that are not reflected in this scintillation index. However, our treatment is consistent with previous treatments of the subject and provides an order of magnitude approximation that bounds the potential effect of scintillation induced by turbulence.

Beam wander is another source of error associated with turbulence[7]. In general, that effect contributes to the estimated horizontal accuracy of the LiDAR sample position (see Table 1). Therefore, beam wander is already accounted for in the error budget. Nonetheless, we have the tools to compute the magnitude of expected beam wander, and do so for the sake of knowledge. Beam wander for a Gaussian beam is described by the parameter r_c, which is shown schematically in Fig. 19.

In our calculations we find that r_c is negligibly small compared with W_e. In the downlink r_c =5x10^{-11}m, and in the uplink it is r_c =3x10^{-10}m.
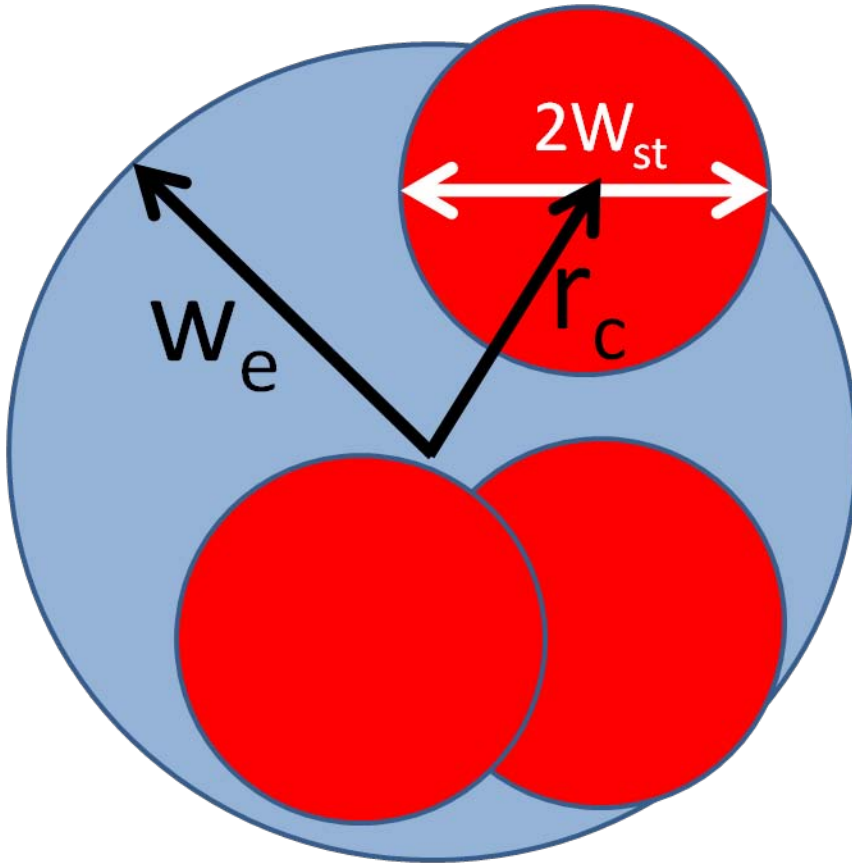

Fig. 19: The shot to shot variation in beam width is characterized by W_{st}. The longer-term beam wander is characterized by r_c. This schematic describes beam wander in the manner described by Ref. 7.

2.3 Target Sampling Model

The sampling model is in some respects similar to a model of darts thrown at a bulls-eye: the laser has limited pointing accuracy and is aimed at a finite-sized target. The sampling laser is modeled as a Gaussian beam. Targets of different physical extent are simulated. The simulation-measured signal is a sum of the signal within the sampled area. The LiDAR problem and the sampling model are displayed schematically in Fig. 20, and in closer detail in Fig. 21.
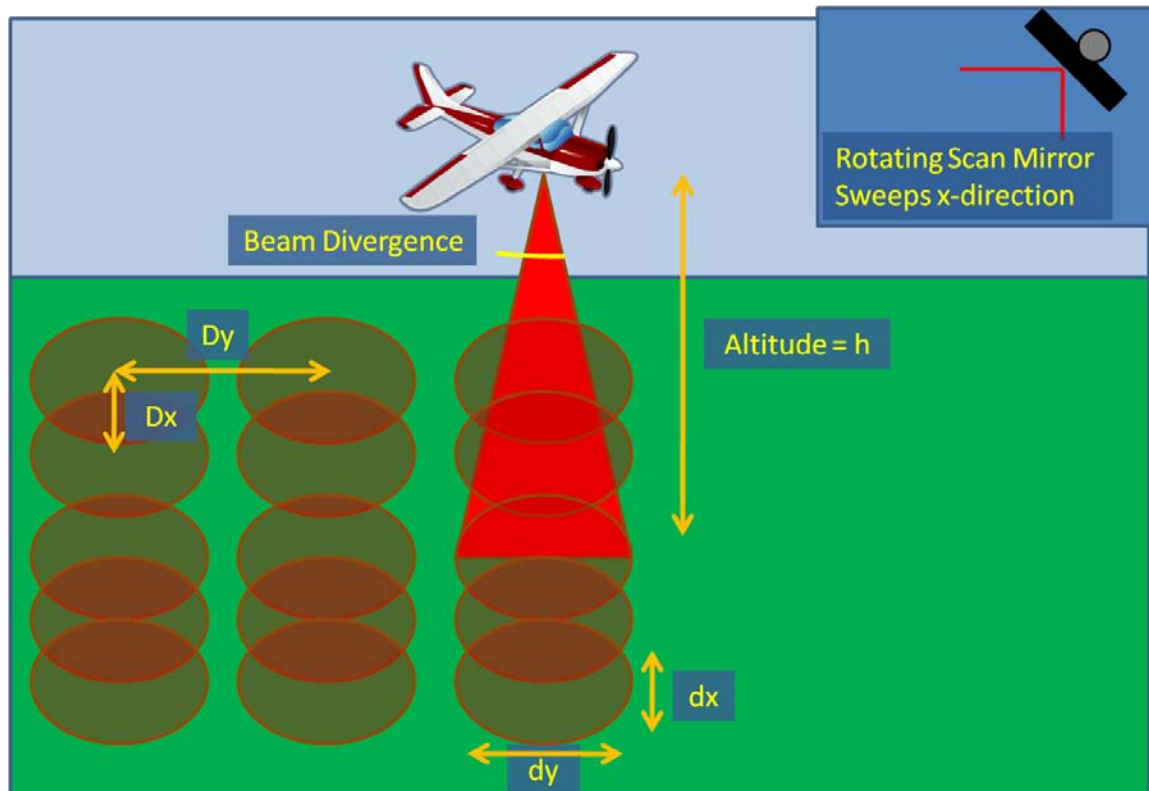

Fig. 20: Schematic of the experimental parameters that contribute to the sample model.
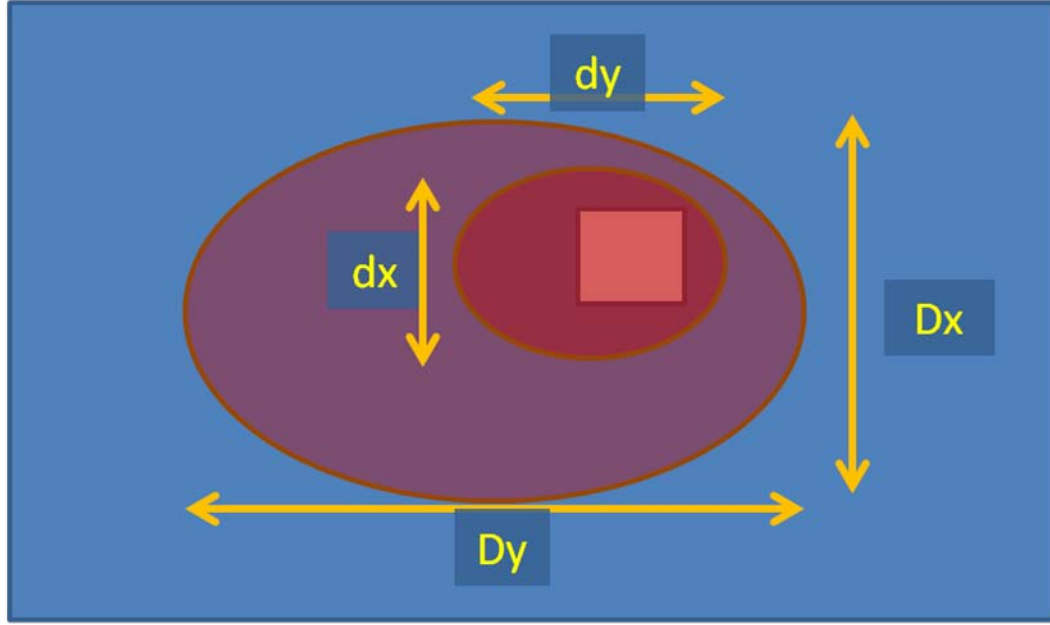
Fig. 21: Detailed schematic where the smaller ellipse represents the laser spot size, the larger ellipse represents the laser pointing accuracy (Dx, Dy), and the rectangle represent a target.

The sample spot size is defined in equations 19 and 20, in terms of the laser pulse width, t_{pw}, the mirror scan rate, Ω, airborne platform's ground velocity, v, and the beam divergence, α:

$$dx = 2h\tan(\alpha/2) + 2h\tan(\tfrac{1}{2}\Omega t_{PW}) \tag{19}$$

$$dy = 2h\tan(\alpha/2) + vt_{PW}. \tag{20}$$

The laser pointing accuracy is defined in the following equations, taking into account the scan mirror's period of oscillation, t_D, in addition to the previously defined parameters:

$$Dx = 2h\tan(\tfrac{1}{2}\Omega t_D) \tag{21}$$

$$Dy = vt_D. \tag{22}$$

Since an area is sampled (the received signal is integrated over the spot size), dx and dy are position uncertainties. Dx and Dy are position inaccuracies, describing the centers of the sample spots. Another contributor to Dx and Dy are geo-positioning errors. And in fact these positional inaccuracies suggest that the target can be completely missed.

The targets are modeled as high-reflectors of size 1ftx1ft, lying in a grassy field. The model uses laser/receiver SNR similar to that seen in data (see table 1 and Fig. 2). Additionally, the model produces signal levels and noise figures that are similar to measured data. Resultant calculations are shown in Figs. 22 and 23. The LiDAR sampling model is developed to study the SNR for both sub-pixel and many pixel detection. When Dy=7ft, Dx=1.4ft, and dx=dy=0.65ft, we expect similar behavior to the NRL-measured LiDAR data. The simulation results are calculated with one free parameter, the total laser energy in appropriate units. The model result maximum is 205DN, simulation-measured mean is 98DN, with standard deviation of 54DN. The experimentally measured LiDAR data average-of-all-targets signal is approximately 100DNs. The measured standard deviation is 77DN. Finally the measured maximum

signal level is 270DN. The simulated standard deviation is small compared with the measured result, but unlike what is modeled here, the measured standard deviation is a total standard deviation, which includes atmospheric factors.

Another parameter that is calculated with this sampling model is Δ_α, which is used in the Ferdinandov models. Here we estimate Δ_α=60%, calculated by dividing the simulated standard deviation by the simulated mean, according to the definition in Ref.[6].
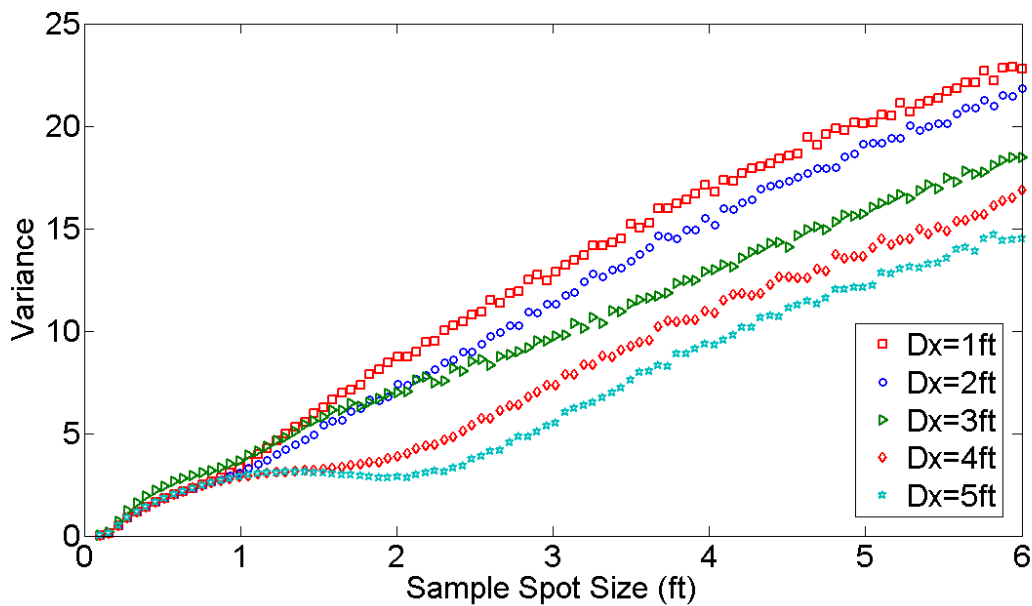

Fig 22: Sampling model computed variance for simulation of a 1ftx1ft target, as a function of spot size for constant Dy=7ft, and several constant values of Dx.
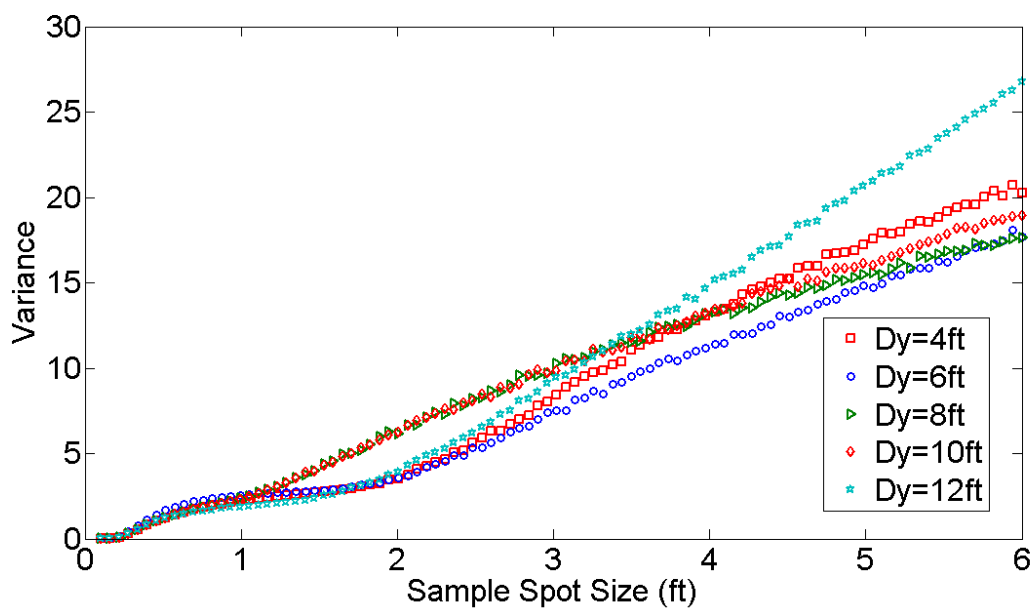
Fig 23: Sampling model computed variance for simulation of a 1ftx1ft target, as a function of spot size for constant Dx=1.4ft, and several constant values of Dy.

3. DISCUSSION OF LiDAR RETRO-REFLECTOR DATA

Applying all of the theoretical tools described and developed in Sec. 2 we can calculate estimates of the total LiDAR measurement variance due to various factors including system noise contributors, atmospheric effects, and experimental sampling errors. For calculation of the total measurement noise we assume that noise factors multiplicatively contribute, in proportion to the normalized noise figure. Multiplicative combination of turbulence and sampling errors is accomplished by:

$$\langle I^2 \rangle = \langle I_{DL}^2 \rangle / \langle I_{DL} \rangle^2 \langle I_{UL}^2 \rangle / \langle I_{UL} \rangle^2 \langle I_{Sampling}^2 \rangle / \langle I_{Sampling} \rangle^2 - \langle I \rangle^2, \qquad (23)$$

where the contributions in variance due to turbulence are due to scintillation in the downlink and uplink channels, as suggested in section 2.2.2.D. This equation simplifies to:

$$\sigma_T^2 = (\sigma_{DL}^2 + 1)(\sigma_{UL}^2 + 1)(\sigma_{Sampling}^2 + 1) - 1. \quad (24)$$

Here σ_{DL}^2 =0.03 and σ_{UL}^2=0.35 are computed via the Andrews and Phillips model (see Sec. 2.2.2D). The average signal and $\sigma_{sampling}^2$=0.30 are computed in Sec. 2.3. Electronics and vibration noise are coupled into the sampling estimate, even though they are not independently represented in Eq. 24. Other errors, such as those attributed to time-independent atmospheric distortion and turbulent-induced beam wander are not included in this total variance estimate, since in Sec. 2.2 they were determined to be negligibly small when compared with the contributors in Eq. 24.

The calculated total noise figure range is σ_T^2=0-0.81. This range covers the measured variance σ_M^2=0.57. Interestingly, neither the variance due to atmospheric turbulence nor the variance due to sampling can independently account for what is observed in the experiment. Combined together via equation 24, these two effects can fully account for the measured variance.

Although the previously described multiplicative combination of signal variances, is consistent with all other assumptions made through-out this paper, it does not account for kurtosis. If kurtosis is present measured intensities could reduce to zero. Ref.[4], indicates the level of kurtosis is small, within the NRL LiDAR data.

As a check on the computation techniques applied here, we perform a variance calculation for the grass background as well. The scintillation induced variance is the same for the grass as it is for the retro-reflectors. In contrast to the retro-reflector calculations, the sampling noise over grass is negligible since the grass is spatially homogeneous. Therefore calculations using Eq. 24 yield a noise figure of σ_T^2=0-0.39. The measured noise figure over grass is σ_M^2=0.26. So again we find that the model results predict numerical values of the normalized variance that bound the measured normalized variance. Interestingly, in both this calculation and the retro-reflector calculation, the measured result is roughly 70% of the max value of σ_T^2's computed range.

If our experiment were better controlled we could use the result that is calculated in previous paragraphs to predict the exact value of the atmospheric structure constant such that $\sigma_T^2 = \sigma_M^2$. Unfortunately, such a calculation would not be meaningful for our present experiment, primarily due to the lack of knowledge about r, the off-axis position at which scintillation should be computed.

Calculations using Ferdinandov's model yield the noise induced by turbulence as an STNR estimate. To obtain a noise figure that approximates the noise induced by scintillation we use the following formula:

$$\sigma_F = \Delta_\varphi \chi (A/r_E) \langle E_H \rangle. \quad (25)$$

In this equation, $\langle E_H \rangle$ =98DN is the mean laser irradiance, and the other parameters are defined and calculated using the Ferdinandov model (see Sec. 2.2.2.B). The result is that for the range of atmospheric structure constants used σ_F=0-28DN. The normalized variance due to atmospheric effects ranges 0-0.28, resulting in σ^2_T=0-0.67 using equation 24. The estimated $SNTR^2$=0-0.77, obtained by applying equation 5 and Δ_α=0.6 (see Sec. 2.3), is yet another estimate for the normalized variance. These values are only in approximate agreement with the values generated by the Andrews and Phillips model and the measurement value σ^2_M. However, the obtained agreement is sufficient to say that the order of magnitude error due to turbulence is approximately 30DN, and certainly smaller than 80DN. Hence with the Ferdinandov model, we find again that a combination of turbulence and sampling are both at play.

Predictive power is perhaps the most interesting aspect of these calculations, in that we can estimate the potential for improvements upon the experiment. For example, if the beam spot size were 1m rather than $1/5^{th}$ of a meter, but all other parameters remain the same, then the measured SNR would be nearly twice as large, 20DN mean divided by 10DN standard deviation as computed with the sampling model. Taking the same set of assumptions, but this time consider when the beam size is nearly 1m, then the simulation-generated total variance is dominated by turbulence noise. Additionally, one could use the equations presented in this paper to aid in optimizing a LiDAR system to reduce turbulence noise. For example, the model of Ferdinandov suggests that an appropriately valued sensor size can aid in reducing the degree of averaging effect χ.

4. CONCLUSIONS

For the NRL LiDAR data described here, measurements of spatially-small retro-reflecting materials are described. In this experiment, as reported previously, a high-level of discrimination between the retro-reflecting targets and the background was found[1]. Although large laser energies are indicated by measurements of retro-reflecting materials, shot-to-shot consistency of the measured intensities is poor. This result suggested the need for a detailed error analysis. A combination of analysis using sensor specific properties, measurements, and modeling suggest that the significant fluctuations observed are caused by a combination of sampling issues and turbulence. Although, the LiDAR sampling employed in the NRL data collect is sufficient to map out large areas of land, it is shown here that sensor pointing inaccuracies negatively affect the sampling of a small retro-reflector. However, understanding of these issues also hints at a simple solution that can make future measurements more reliable. This information in addition to the estimations on turbulence and other noise contributors are all valuable in our continuing development of LiDAR detection of small retro-reflectors.

ACKNOWLEDGMENTS

REFERENCES

1) P. Lebow, J. Neumann, J. Murray-Krezan, J. Ackerman, A. Huston, and B. Wright, "Active Illumination and Spectral Discrimination of Retro-reflective Targets in Remote Sensing Systems," *Proceedings of the 2009 MSS Passive Sensors Symposium*, (2009).

2) L.J. Lego Jr, "Search and Located System," U.S. Patent 4,131,791 (1978); K.G. Wesolowicz, D.S. Dilworth, R.W. Zywicki, K.A. More, J.P. Lehotsky, F.G. Osterwisch, "Target Detection System Utilizing Multiple Optical Criteria," U.S. Patent 5,739,034 (1998).

3) "ALTM2025 Specifications," Optech Inc., Toronto ON, 2002.

4) "LiDAR Mapping Report," Airborne 1 Corp. , El Segundo CA, 2008 (unpublished).

5) A. Wehr and U. Lohr, "Airborne laser scanning-an introduction and overview," *ISPRS Journal of Photogrammetry and Remote Sensing* **54**, 68-82 (1999).

6) E. S. Ferdinandov, V. I. Tsanev, and B. O. Todorov, "Turbulence-Noise in Infrared LiDAR Sensing," *Infrared Phys. Technology*, **36**, 105-111 (1995).

7) L. C. Andrews and R. L. Phillips, *Laser Beam Propagation Through Random Media* (SPIE Optical Engineering Press, Bellingham, WA, 1998).

8) A. Yariv, *Quantum Electronics 3rd Ed.* (John Wiley and Sons, New York, 1989).

9) J.L. Bufton, R.S. Iyer, and L.S. Taylor, "Scintillation statistics caused by atmospheric turbulence and speckle in satellite laser ranging," Applied Optics **16**, 2408-2413 (1977).